Paul R. Medwell, Peter A.M. Kalt and Bassam B. Dally
Simultaneous imaging of OH, formaldehyde, and temperature of turbulent nonpremixed jet flames in a heated and diluted coflow
Combustion and Flame, 2007; 148(1-2):48-61

Full-length article:

Simultaneous Imaging of OH, Formaldehyde and Temperature of Turbulent Nonpremixed Jet Flames in a Heated and Diluted Coflow

Shortened running title:

Jet Flames in a Heated and Diluted Coflow

Paul R. Medwell *, Peter A. M. Kalt and Bassam B. Dally

School of Mechanical Engineering, The University of Adelaide, S.A. 5005 Australia

Abstract

This paper reports on measurements in turbulent nonpremixed CH_4/H_2 jet flames issuing into a heated and highly diluted coflow. These conditions emulate those of Moderate and Intense Low oxygen Dilution (MILD) combustion. The spatial distribution of the hydroxyl radical (OH), formaldehyde (H_2CO) and temperature, imaged using Planar Laser Induced Fluorescence and Rayleigh Scattering laser diagnostic techniques, are measured and presented. Comparisons are made between three jet Reynolds numbers and two coflow O_2 levels. Measurements are taken at two downstream locations. The burner used in this work facilitates the additional study on the effects of the entrainment of surrounding air on the flame structure at downstream locations. Reducing the coflow oxygen level is shown to lead to a suppression of OH as a result of the reduced temperatures in the reaction zone. Decreasing the oxygen level of the coflow also results in a broadening of the OH distribution. At downstream locations, the surrounding air mixes with the jet and coflow. The subsequent drop in the temperature of the oxidant stream can lead to a rupture of the OH layer. Localised extinction allows premixing of the fuel with the surrounding air. The result is an increase in the reaction rate, highlighting the need for homogeneous mixing to maintain MILD combustion conditions.

Key words: MILD, Nonpremixed, OH, Formaldehyde, Rayleigh

* Corresponding Author. Tel: +61 8 8303 3157; Fax: +61 8 8303 4367
Email addresses: paul.medwell@adelaide.edu.au (Paul R. Medwell), pkalt@mecheng.adelaide.edu.au (Peter A. M. Kalt), bassam.dally@adelaide.edu.au (Bassam B. Dally).

1 Introduction

Heat and exhaust gas recirculation in combustors is an innovative approach to create a distributed reaction zone, reduce pollutant emissions and increase the net radiation flux, and with it thermal efficiency. It is now well established that a mixture of reactants diluted with combustion products, at a temperature above auto-ignition, can achieve the desired outcome of reduced pollutant emissions and enhanced thermal efficiency. The application of these principles to practical systems has taken different routes and different names used to describe the process. Some relied on a descriptive form of the resulting combustion process, i.e. Flameless Oxidation [1] and others described the features of the reactants streams, i.e. High Temperature Air Combustion. The term used in this paper is Moderate and Intense Low oxygen Dilution (MILD) combustion [2].

The MILD combustion technology has been successfully applied in several industries [3], and has the potential for introduction into numerous other applications [2]. To date however, implementation has been impeded by a lack of fundamental understanding of the establishment and detailed structure of this combustion regime. Few fundamental studies have been performed to look at the detailed structure of this regime (e.g. [2, 4, 5]).

Dally *et al.* [4, 6] reported on the structure of hydrocarbon nonpremixed laminar and turbulent flames stabilised on a jet in a heated and diluted coflow. They used single-point Raman-Rayleigh-LIF diagnostic techniques to simultaneously measure temperature, major and minor species at different locations in these flames. They found that major changes in the flame structure occur when reducing the oxygen concentration and that, at higher jet Reynolds number and low oxygen con-

centration, oxygen leakage from the surroundings may cause local extinction of the flame.

Ahn *et al.* [5] reported on a heated and diluted jet of premixed methane fuel propagating against its products. The jet impinges on a cup that circulates the products back to the jet exit before it is exhausted from the side. Temperature was measured using a thermocouple and turbulence quantities were measured using Laser Doppler Velocimetry. The authors showed that increasing the Karlovitz number (Ka) from $\sim$0.44 to 1.72 caused the PDF of temperature to change from Gaussian to a bimodal distribution. They also argued that the current criteria for the transition from thin reaction zone regime to broken reaction zone regime needed to be modified when applied to a preheated and diluted mixtures.

The current project aims to examine the structure of the reaction zone of a jet in a heated and diluted coflow using planar laser imaging techniques. Temperature, the hydroxyl radical and formaldehyde are measured instantaneously and simultaneously at different parts of the flames. The hydroxyl radical (OH) is used as flame marker while the formaldehyde (H_2CO) intermediate species is predominant at low temperatures typical of those found in MILD combustion. The product of $[OH]$ and $[H_2CO]$ has also been suggested as an indicator of the formyl (HCO) radical, which is closely related to the heat release rate [7].

In this paper we report on the combination of the three scalars in turbulent non-premixed CH_4/H_2 flames stabilised on a jet issuing into a heated and diluted coflow. The jet in hot coflow burner emulates MILD combustion under controlled conditions. Comparisons are made between three jet Reynolds numbers and two coflow oxygen levels. Measurements are taken at two downstream locations. The burner used in this work facilitates the additional study of the effects of the entrainment of

surrounding air on the flame structure at downstream locations.

2 Experimental Setup

The MILD combustion burner used in this study is similar to the jet in hot coflow (JHC) burner used elsewhere [4], in that it consists of a central insulated fuel jet ($\varnothing$4.6mm) within an annular coflow ($\varnothing$82mm) of hot exhaust products. In the current design however, a porous bed burner mounted upstream of the jet exit plane replaces the secondary burner [8, 9] as shown in Figure 1. The fuel jet is more than 100 diameters in length to ensure fully developed pipe flow. The outer annulus is insulated with a fibrous blanket to minimise heat losses to the surrounds. The influences of the coflow remain $\sim$100mm downstream of the jet exit plane, beyond this the surrounding air begins to mix with the jet and coflow. The surrounding air entrainment facilitates the additional study of these effects on the reaction zone.

The fuel used in the jet is natural gas (92% CH_4 by volume) diluted with H_2 in equal volumetric parts. The O_2 level of the coflow is controlled by the constant flowrate secondary porous burner. The ratio of the coflow air/nitrogen was varied to give excess O_2 levels of 3% or 9% (volumetric), while the coflow temperature and exit velocity was kept constant at 1100K and 2.3m/s. Based on the annulus diameter the coflow Reynolds number is $\sim$1400. Investigated flame conditions and visible flame lengths are presented in Table 1. The jet Reynolds numbers are based on the jet inner diameter.

Laser induced fluorescence (LIF) is used to image OH and H_2CO, and temperature is inferred from Rayleigh light scatter measurements. Each species is probed with a separate laser system. Excitation of OH is at 283.222nm $(A - X\ (1,0)\ Q_1(7))$,

and H_2CO via $A - X\ (2_0^1 4_0^1)\ ^pQ_{21}(5)$ at 340.836nm. The two LIF laser beams were produced from the frequency doubled output of dye lasers (Nd:YAG pumped at 532nm). The output power of the dye lasers was $\sim$2mJ/pulse for OH and $\sim$10mJ/pulse for H_2CO, with measured linewidths of 0.5cm^{-1} and 0.26cm^{-1} for OH and H_2CO, respectively. The source for the Rayleigh scatter was a $\sim$160mJ/pulse 532nm beam from a Nd:YAG laser.

The OH–LIF excitation scheme was chosen to minimise the variation in ground-state Boltzmann fraction population distribution over the expected temperature range, based on the rotational and vibrational energy level expressions of Dieke & Crosswhite [10]. For the H_2CO molecule both the rotational and vibrational energy terms have a significant influence on the ground-state population distribution. The selected H_2CO vibrational excitation band $(\mathrm{viz.}\ 2_0^1 4_0^1)$ has been shown to be the most advantageous in terms of signal strength [11]. The H_2CO–LIF rotational excitation was chosen based on a compromise of maximising the ground-state rotational distribution whilst minimising the variation with temperature. Additional consideration is given to the rotational branch intensity based on the intensity factors given in Dieke & Kistiakowsky [12]. It is assumed that H_2CO is a symmetric top (asymmetry parameter, $\kappa = -0.96$ [13]) in calculating the rotational energy levels based on the energy expression of Atkins [14]. Vibrational energy levels from Maessen & Wolfsberg [15] are used in conjunction with the rotational energy levels to calculate the Boltzmann population fractions. The variation of the Boltzmann population fractions with temperature for both OH and H_2CO are plotted in Figure 2

The experimental layout is shown in Figure 3. The three laser wavelengths are formed into overlapping co-planar laser sheets. The laser sheets pass through a laminar slot burner (for reference purposes) in the same field of view as the JHC

burner. The laser pulses are fired sequentially to reduce interferences on the other systems. Each species is detected normal to the laser sheet with a gated intensified CCD (ICCD) camera. To accommodate three separate cameras, a dichroic mirror is used between the OH and Rayleigh cameras. The dichroic reflectance is greater than 80% in the range 270–340nm, therefore acting as a broadband filter for the OH camera. The H_2CO and Rayleigh cameras were each fitted with long wave pass optical filters, GG-385 and GG-495 respectively. To minimise elastic scatter from particulate matter, gases were filtered and measurement locations chosen which were free of visible soot. The Rayleigh and H_2CO cameras were both used with $f_{\#}1.2$ lenses, and OH with a $f_{\#}4.5$ lens. The in-plane resolution of all three ICCD cameras is 160µm, after spatial matching. The light sheet thicknesses are estimated to be slightly larger than this, but of a similar order based on burns from photosensitive paper. The laser sheet heights were all $\sim$12mm, of which the central 8mm portion is presented herein.

3 Data Analysis

The images from the three ICCDs are spatially matched typically to sub-pixel accuracy, however the worst case mismatch is never more than 2 pixels (320µm). Each image is corrected for dark-charge, background and detector attenuation. All images are corrected for laser power and profile variations shot-to-shot based on the signal from the laminar slot burner. Based on the measurements from a flat-flame burner, the laser power shot-to-shot corrections result in intershot variations of $\lesssim$5% for the OH and temperature. H_2CO shot-to-shot variations could not be accurately determined, but are expected to be of a similar order to the others. Approximately 400 images are recorded at each flame location and condition.

The signal to noise (SNR) of the instantaneous corrected images is typically better than 40:1 for OH, 10:1 for Rayleigh and 5:1 for H_2CO. The authors acknowledge that higher SNR for H_2CO would have been desirable. Being a polyatomic molecule, H_2CO–LIF is inherently weak as the population is distributed over a large number of quantum states. Weak H_2CO–LIF is compounded in nonpremixed flames due to the low H_2CO concentrations in comparison to premixed and partially premixed flames. It is also noted that the H_2CO signal suffers only minor encroachment of vibrational Stokes-shifted Raman scatter from H_2 passing the detection filter. This interference is restricted to radial locations close to the centreline and has little effect near the flame location. Despite these issues, the H_2CO–LIF is sufficient to obtain reasonable understanding of the parameters that control its concentration and spatial distribution.

3.1 Temperature (Rayleigh scatter)

Converting the Rayleigh response to temperature was achieved through estimates of the Rayleigh cross-sections in the fuel and coflow streams, based on the **major species** composition of the calculated laminar nonpremixed flames over a range of strain rates using the OPPDIF code of the Chemkin package and the GRI-Mech version 3.0 mechanism. The location of peak OH is used to demarcate coflow from jet fluid. The models indicate that the Rayleigh cross-section on the lean side of the OH peak to the coflow is effectively constant. The lean side of the OH boundary is therefore assigned a constant Rayleigh cross-section. On the fuel rich side, a series of intermediate levels of Rayleigh cross-section are used between the OH peak and the jet. For this process the jet is defined as the region with the highest Rayleigh scatter (the unreacted fuel jet will have lowest temperature and also high-

est Rayleigh cross-section, both leading to strong elastic scattering). This method to account for differential Rayleigh cross-section makes the assumption that the imaged jet fluid consists of pure fuel at the measurement location. This is a reasonable assumption for the 35mm downstream measurements, although potentially less so at 125mm downstream. Based on the laminar nonpremixed flame calculations the Rayleigh cross-section variations are found to be at most 20%, even at the downstream location.

3.2 Hydroxyl radical (OH–LIF)

The OH–LIF from the jet is quantified based on the signal from the reference flame imaged in the same field of view. In the linear LIF regime, number density may be expressed as [16];

$$n = n_{cal}\left[\frac{I}{I_{cal}} \cdot \frac{F_{cal}}{F} \cdot \frac{E_{L,cal}}{E_L} \cdot \frac{Q}{Q_{cal}} \cdot \frac{g(\nu_0)_{cal}}{g(\nu_0)}\right] \tag{1}$$

For the present experiment, the subscript cal refers to the calibration laminar slot burner flame, n is the OH number density, I the LIF intensity, F the Boltzmann fraction, E_L the laser energy, Q the quenching rate and $g(\nu_0)$ the spectral overlap.

The particular OH–LIF excitation scheme outlined in the experimental section (§2) was chosen such that, over the temperature range of interest, variation in Boltzmann fraction is small ($\lesssim$10%) and is considered negligible. Given the similarity of the jet flame and the laminar diffusion reference flame, the spectral overlap term is also considered negligible. The ratio of the laser energy is accounted for when corrections are made for the sheet profile variations. The remaining terms are the ratios of the LIF intensity and the quenching rates. LIF intensity is readily obtained

from the images. Corrections for the quenching rates are made based on the major species composition obtained from laminar nonpremixed flame calculations using the OPPDIF code of the Chemkin package and the GRI-Mech 3.0 mechanism in conjunction with collisional quenching cross-sections obtained from Garland & Crosley [17]. Over a wide range of strain rates, the quenching rate for each of the flames remains almost constant throughout the region of interest. Uncertainty of the quenching rate due to strain variations on the composition are at most 10%, and typically less than this.

Verification of the OH quantification technique was achieved by replacing the JHC nonpremixed flame with a premixed flat-flame. Agreement between the experimentally determined OH number density in the flat-flame and that predicted by the Chemkin models is better than 95% [18].

3.3 Formaldehyde (H_2CO–LIF)

Pseudo-quantitative data are used to investigate the spatial distribution of H_2CO. As such, the H_2CO data presented herein is only indicative of the species concentrations. Lack of detailed information on the quenching of H_2CO prevents quantification. However, the similarity of the quenching environment of the combustion products and the coflow suggests that the relaxation rates should be similar throughout the region of interest, as was shown for OH. Furthermore, it has been suggested that there is negligible difference in assuming a constant H_2CO quenching cross-section compared to applying a temperature dependent model for the quenching [19]. As a result of the large variation of H_2CO population distribution with temperature, corrections are made to the H_2CO–LIF images using the corresponding temperature image and the Boltzmann population fraction function shown in Figure 2. With the

corrections for Boltzmann distribution and the assumption of uniform quenching environment, the relative intensities of the LIF signals gives a reasonable estimate of the relative concentrations.

The H_2CO images appearing within this paper have been smoothed using a 3×3 median filter. The other images have not been enhanced by image smoothing to reduce inter-pixel noise.

4 Results and Discussion

4.1 Visual observations

Figure 4 shows photographs of the flames presented in this paper. It is clear that the flames have different features at the two measurement locations indicated, namely 35mm and 125mm above the fuel jet exit plane. These locations were chosen to represent two oxidant regimes. At the 35mm location, the oxidant stream is that of the coflow (with a specified O_2 level) while at the 125mm location air from the surrounds is entrained with the coflow stream resulting in a different oxidant composition than at the 35mm location. Noteworthy is that the flames with 3% O_2 in the coflow are virtually free of visible soot for the full length of the flame. While for the 9% case soot appears at around 250mm above the jet exit. This points to the fact that kinetics play a major role in the soot formation path in these flames especially considering the Reynolds number is the same for the two different coflow streams. **In all cases the total visible flame length at 3% O_2 is longer, with differences more noticeable at lower Re_{jet}, as shown in Table 1.**

4.2 Instantaneous images: 35mm downstream

Figures 5a and 5b show typical instantaneous image triplets of OH, H_2CO and temperature at the 35mm location for two coflow stream O_2 levels. **These images are for a jet Reynolds number of 15,000 and are typical of other Reynolds numbers as well.** The corresponding size of each image is 8×30 mm. The spatial location of H_2CO on the fuel-rich side, in relation to OH, reinforces that H_2CO is a first-step intermediate [20] formed as a product of fuel decomposition [21]. The temperature images show a uniform temperature distribution in the coflow stream, and for the 9% O_2 coflow a distinct peak close to the reaction zone. For the 3% O_2 case the temperature peak is barely discernable, however a definite OH layer is measured, albeit at lower OH levels than for the 9% case.

At different Reynolds numbers the images show similar features. Nonetheless, at higher Re_{jet} a greater proportion of the instantaneous images show signs of convolution and weakening of the OH distribution, examples of which are shown in Figures 5c and 5d. In images where the OH is reduced, the H_2CO levels show a noticeable increase. The reduction in reaction rates at low O_2 levels and the weakening of OH and subsequent increases in H_2CO are more noticeable with a 3% O_2 coflow.

Partial premixing has been shown to significantly increase H_2CO levels in hydrocarbon flames [22, 23]. Figure 7 presents peak H_2CO mole fractions using the OPPDIF code of the Chemkin package and the GRI-Mech 3.0 mechanism for a single fixed flow velocity at various fuel stream equivalence ratios beyond the fuel-rich limit. For either oxidant stream composition it is clearly apparent that increasing the level of partial premixing leads to a significant increase in

the peak H_2CO concentration. At stoichiometric conditions ($\Phi = 1$) the peak H_2CO level has also been determined using the PREMIX code of the Chemkin package and again the GRI-Mech 3.0 mechanism

Figures 6a and 6b show images with very strong H_2CO on the oxidant side of the reaction zone. **Based on visual observation of the the images where H_2CO is seen to exist on the oxidant side of the reaction zone, the frequency of such mixing events is $\sim$1.1%, $\sim$4.4% and $\sim$5.1%, in ascending order of the three Reynolds numbers considered in this paper (Table 1).**

Estimates of the mean thickness (FWHM) of the OH layer from the instantaneous images are shown in Table 2. **This table is generated by examining the full-width half-maximum in each row of each image and then averaging. As expected, the reduced oxygen concentration requires a greater volume of oxidant stream to consume the fuel, as such the 3% O_2 coflow flames have a thicker OH width as compared to the 9% O_2 case. The thickness increases slightly with Reynolds number, consistent with previous work [24]. The variation in the OH width with Reynolds number is less than the resolution of the measurement system, there is however a clear trend. The less prevalent increase in thickness with Reynolds number at the lower O_2 level may possibly be due to an increased decay of turbulence levels under these diluted conditions.**

4.3 Mean and RMS radial profiles at axial location 35mm downstream

Figure 8 shows the mean and RMS radial profiles of OH, H_2CO, and temperature for both 3% and 9% O_2 at various jet Reynolds numbers, and at an axial location of 35mm above the jet exit plane. **Each plot is generated only from the central**

3mm strip of the images, and not from the entire sheet height. From this figure it is clear that reducing the O_2 levels leads to a substantial suppression of OH as already seen in the instantaneous images of Figure 5. This observation is consistent with previous work (e.g. [25]) and is directly related to the reduced temperature of the reaction zone. The 3% O_2 coflow case shows a radial shift of the OH peak towards the oxidant stream of $\sim$1mm in relation to the 9% O_2 case. Also apparent is that the Reynolds number does not seem to have a significant influence on the mean or RMS profiles of OH at either O_2 level, although minor differences are apparent at the 9% coflow. It is also noted that minor equilibrium OH levels in the coflow stream are observed at both coflow conditions.

An increase in Re_{jet} has the most marked effect on H_2CO mean profiles. Between Re_{jet} = 5000 and 15000, the mean H_2CO increases by a factor of $\sim$4.4 for the 3% O_2 coflow case and $\sim$10.4 for the 9% O_2 case. A similar trend has been observed in the strained laminar nonpremixed flame calculations we have performed, and has also been briefly noted by others [26], though not quite to the extent observed here. The broad radial profile distributions of H_2CO presented here are consistent with previously reported nonpremixed flames [26, 27].

As already seen from the instantaneous images (Figures 6a & 6b), transfer of jet fluid into the coflow results in significant increases in H_2CO levels. This is reflected in the H_2CO RMS profiles of Figure 8. At 3% O_2 there is a much higher H_2CO RMS at wider radial locations, indicating a greater proportion of unreacted jet fluid penetrating the reaction zone. This is directly related to the less intense reaction zone at the lower O_2 level, whereby fuel is able to pass through the flame front without being completely consumed.

Due to the low O_2 levels, the temperature peak under MILD combustion conditions

is expected to be only slightly above the coflow temperature. As expected from the instantaneous images, in the mean there is no clear discernible peak for the 3% O_2 coflow case despite the OH clearly indicating a reaction taking place. For the higher 9% coflow case, the mean temperature rise is only 200–400K. It is worth noting that the peak temperatures are lower than what has been previously reported by Dally *et al.* [4], and may be primarily attributed due to the lower temperature coflow used in the present study (1100K compared to 1300K).

The influence of Re_{jet} on both OH and temperature is quite minor at this location. Both the mean and RMS levels of OH remain essentially constant over Re_{jet} = 5000 – 15000, however a slight (1mm) outward radial offset of the OH peak location is observed for the lowest Re_{jet} at 9% O_2 coflow. Similarly, the temperature profiles are consistent, again with only slight variations being noted at the lowest Re_{jet}. The RMS of the temperature is relatively low in the shear layer, even at high Re_{jet}.

4.4 Results from axial location 125mm downstream

At 125mm downstream it is visibly evident that the flames are perceptibly different in structure, as seen in Figure 4. At this location the surrounding air is able to penetrate the coflow, subsequently having an influence on the flame structure. There remains clear differences between the 3% and 9% O_2 coflow cases at this location however, particularly evident in the differing mean profiles of the H_2CO seen in Figure 9. **As highlighted previously for Figure 8, Figure 9 is generated only from the central 3mm strip of the images, and not from the entire sheet height.** Mean plots of OH and temperature again show minor differences with Re_{jet} for either coflow case. Differences in the peak temperatures between O_2 levels are $\sim$250K and $\sim$100K along the centreline. The RMS of the OH and H_2CO at this

location in percentage terms are approximately double those at 35mm downstream. As expected, at this 125mm downstream location the radial profiles are significantly broader than for the 35mm radial plots of Figure 8. The temperature profiles of Figure 9 clearly indicate that the influence of the coflow has diminished at this downstream location as evident by the low temperatures at wider radial locations. For the 9% O_2 at this location the trend of H_2CO increasing with Reynolds number is reversed in relation to what is seen in the other measurements. Occasionally the H_2CO signal in this image set is seen to be much higher than typical levels, having the effect of skewing the mean and is clearly apparent in the very high RMS of the low Re_{jet} cases.

From the photographs of Figure 4 the effects of the coflow seem to effect the visual appearance of the flame $\sim$100mm downstream of the exit plane for the 3% O_2 case, whereas at 9% the coflow influences seem to remain $\gtrsim$200mm. As already reflected in the temperature and OH measurements, the 9% O_2 coflow is expected to have an increased reaction intensity due to the higher oxygen concentration. The more resilient reaction zone seems to provide a more significant barrier between the jet and oxidant streams. Consequently the effects of the surrounding air for the 9% O_2 flame do not appear until further downstream than for the 3% case. The enhanced mixing at the higher Reynolds number conditions increases the interactions of the surrounding air and the reaction zone.

The entrainment of cold air at the downstream location (125mm) has a substantial effect on the reaction zone for both of the examined coflow O_2 levels, most significantly at the 3% O_2 case. With the inclusion of surrounding air, the associated drop in temperature can lead to a local extinction of the flame front, based on the OH and temperature images. The nature of such extinction events is attributed to cooling.

An example of extinction due to cooling is evident in Figure 10a. The image triplet shows a cold region of entrained air from the oxidant side (righthand side) and rupture of the flame front in the OH image. The subsequent break in the flame front has allowed fuel to mix with the air, and the elevated temperature in this region ($\sim$900K) has initiated a premixed flame, evident by the increased H_2CO levels in the area adjacent to the OH break.

Whilst cold air coming into contact with the reaction zone can lead to extinction, the higher O_2 level of the air can also lead to an increase in the reaction intensity (increases in both OH and the local temperature), as evident in the non-extinguished parts of image Figure 10a.

It is proposed that the effects of the surrounding cool air at the downstream location takes place in a consecutive of steps. The first step is the extinction due to cooling by the surrounding air. The subsequent rupture of the reaction zone allows the fuel and the air to premix. The partially premixed region ignites, evident by the H_2CO levels increasing. Due to the increased oxygen levels this newly formed reaction zone has a higher reaction intensity and subsequently higher OH and temperature.

The trend of entraining surrounding air tending to increase H_2CO levels and subsequently OH and temperature occurs at the 9% O_2 coflow as well. At this higher O_2 level, the strengthened reaction zone tends to make the flame front far more resilient to rupture by these entrainment events. The effect of air entrainment increasing the H_2CO due to premixing and the resultant increases in OH and temperature may still be noted at the 9% O_2 coflow in Figure 10b. Although the inclusion of higher O_2 air may tend to increase the OH and temperature due to increased reaction rates, until they adequately mix the O_2 influence does not necessarily increase the OH and temperature, as shown in Figure 11a.

Extinction of the flame front due to cooling does not necessarily require room temperature air, rather a lower temperature region. Figure 11b is an example of this. Here, a cooler (but not cold, T$\sim$550K) region may be seen between and beneath the two small regions of OH, and it is this lower temperature which is believed responsible for this extinction event. Again, associated with this extinction is the interaction of the fuel and oxidant giving rise to a premixed region evident by the strong H_2CO. The comparatively low signal of each species indicates that this is a recent extinction event, whereby the premixed flame has not yet had a sufficient opportunity to increase the OH and temperature.

Figure 11c shows another example of an extinction event. This time however it appears to be towards the end of it, whereby the OH appears to be dominating and the higher temperatures indicate that the reaction has recovered following a re-ignition. Only a small premixed pocket remains where the H_2CO persists. Despite an extinction event via cooling (albeit not by entirely cold room air), the flame front has re-established. Figure 11d also shows another extinction event where the OH and temperature have recovered. The strong H_2CO present in this image is expected to soon be consumed.

A largescale vortex is noted in Figure 11e. The H_2CO island at a wider radial location than the OH indicates that fuel is present on this outer side. The higher temperatures on the inner side of the OH tends to suggest that this region has in fact been coflow which has been forced towards the jet centreline. The high temperature and low O_2 level of the oxidant results in the OH levels being comparable to the controlled 3% O_2 flames at the 35mm downstream location. This image therefore indicates that a disturbed flame front can retain the features of a controlled flame providing the local environment is suitable.

Figure 11f shows examples of both situations in the extinction cycle. On the outer side, cold fresh air has lead to a rupture of the OH, enabling a small pocket of premixing, and the production of H_2CO, indicating that fuel has reached the cold air surrounds. Temperatures on this side, even where OH is present, are low. Overall, this appears to be indicative of a recent extinction event. On the jet side of the high temperature region, a much stronger band of OH is seen. Just to the inside of the strong OH and temperature, the presence of strong H_2CO and a corresponding region of cooler temperatures tends to indicate that in this area surrounding air has been entrained which caused a brief extinction, followed by premixing and consequently leading to the higher OH and temperature on this side of the image.

Overall, the extinction events identified do not indicate that the entire flame becomes extinct. Rather the flame front becomes locally and instantaneously broken. The localised extinction is accompanied by the formation of H_2CO, indicating that the reaction has recommenced. This re-ignition process is initiated by the heated coflow, which acts as a pilot. Although there is evidence of cold surrounding air penetrating the coflow and leading to temporary extinction at the downstream locations, there are enough hot products to ensure a sufficient temperature to sustain the overall reaction.

Although no extinction events are seen at the higher (9%) O_2 case, similar trends relating to surrounding air entrainment may be observed in the images. For example, Figure 10b shows evidence of entrained cooler air and subsequent premixing which has lead to the island of high H_2CO, surrounded by high OH and temperature – exactly the same as noted for the 3% O_2 cases. The difference at the higher oxygen levels is that the initial reaction zone is more intense, consequently, the entrainment of surrounding air serves only to weaken the reaction zone rather than to cause extinction. An example of the weakened reaction zone at the 9% O_2 coflow

is seen in Figure 12a. As a result of the weakened (but not extinguished) reaction zone, oxygen leakage from the surrounding air has penetrated the flame front. This in turn has lead to an increase in H_2CO in the vicinity of the weakened OH.

Even in situations where there is not necessarily cold air “pockets”, but clearly there has been some form of surrounding air entrainment as indicated by the strong H_2CO levels, the OH and temperature levels still increase markedly, as seen in Figures 11d and 12b.

5 Discussion

At the downstream location, the instantaneous images presented suggest that the entrainment of surrounding air can lead to localised extinction of the reaction zone by means of cooling. It is surmised that the extinction process goes through the following stages;

- Cold (cool) air from the surrounds causes a localised break in the flame front, indicated by a rupture of the OH
- Fuel, coflow and the surrounding air mix, leading a to local premixed region
- The elevated temperatures result in ignition of the premixed pocket. A premixed reaction is evident by high H_2CO levels
- The additional oxygen concentration within the premixed pocket subsequently leads to a higher intensity reaction than the nonpremixed flame front, resulting in higher OH and temperature

The suggestion that extinction is by cooling is brought about by the associated decreases in temperature in conjunction with the increase of H_2CO in such images. In the images with apparent local extinction a region can be identified with evidence

of entrainment, typically with lower temperatures. The presence of strong H_2CO at the location of extinction events is suggestive of premixing with greater oxygen levels than in the coflow stream, suggesting interaction with the surrounding air. The H_2CO which is seen in the instances of local extinction suggests that these extinction effects are genuine and not falsely identified due to out-of-plane effects, which are minimised due to the streaming nature of this flow.

Based on analysis of the image set, the proportion of images with evidence of extinction is shown in Table 3. The increased frequency of extinction events with increased Reynolds number may initially appear to point towards strain induced extinction. From the evidence seen in these images, as already outlined, it is speculated that cooling leads to these extinction events rather than strain. The frequency of extinction increasing with Reynolds number is attributed to increased mixing, entraining more surrounding air and so leading to a higher frequency of extinction events. This conclusion is reinforced by the observation that the extinction events at all Reynolds numbers have the same structure – it is merely the frequency of extinction that changes with Reynolds number. Further evidence that strain is unlikely to lead to extinction is noted in laminar flame calculations. Heating of the oxidant stream raises the extinction strain rates to higher levels than possible for a 21% O_2, and 300K temperature in the oxidant stream.

The intimation that at the downstream location localised extinction takes place via cooling has previously been suggested in turbulent jet piloted diffusion flames and bluff-body flames [24, 28].

Having identified from Table 3 that Reynolds number has a significant effect on the extinction processes at the 3% O_2 case, it would be expected that the OH RMS plots of Figure 9 would reflect this as well. Figure 9 reveals a significant variation

in the 3% O_2 OH RMS peak and radial width of the RMS profiles, such that the total RMS is significantly higher at increased Reynolds number. The differences with Reynolds number in Figure 9 may not seem as substantial as expected based on the statistics presented in Table 3, however. This difference is due the different sheet heights used to construct each of these data results. For the statistics of Table 3 the entire image height (8mm) was used to determine extinction events, whereas for Figure 9 only a radial strip 3mm high at the identified axial distance was used, thereby reducing the likelihood of an extinction event occurring within this narrower region.

Near the jet exit, where the oxidant composition is entirely controlled by the hot coflow, it has been shown that a reduction in O_2 concentration leads to a suppression of OH, directly related to the drop in temperature. Another consequence of reducing the O_2 level is slight broadening of the width of the OH surface.

Reynolds number effects on the structure of these flames appears minimal based on the mean and RMS radial profiles at either axial location. The maximum of these plots does not necessarily represent the mean peak OH number density however, as a result of the inherent spatial averaging. Instead, from each image the peak OH number density has been determined. The mean of the peak from each image gives a better indication of the mean peak OH number density. Shown in Table 4 is the mean of the peak OH value in each of the images in the set, also presented is the standard deviation of these peak values throughout the set.

As already noted in the mean OH plots of Figures 8 & 9, Table 4 reinforces that the coflow O_2 level dramatically affects the OH, with OH levels doubling from the 3% to 9% coflow. A feature noted in Table 4 which was not seen in the mean radial plots however is the increase of mean peak OH number density at the downstream

location. For the 3% O_2 coflow, the peak OH number density in the radial plots dropped from $\sim 0.45 \times 10^{16}$ cm^{-3} at the 35mm location to $\sim 0.25 \times 10^{16}$ cm^{-3} at the 125mm downstream location, and is largely independent on Reynolds number. Whereas Table 4 shows the opposite trend of an increase in the mean peak OH further downstream and this increase is highly dependent on the Reynolds number. The difference between the two downstream locations is due largely to the effects of the surrounding air entrainment. The additional O_2 levels as a result of the entrainment leads to an increase in the OH, as already noted in the instantaneous images. This effect is masked in the radial plots due to the spatial averaging.

Close to the jet exit (35mm location), as expected, the standard deviation of the OH number density is quite low ($\sim$10%) for either coflow or Reynolds number. Further downstream the interactions with the surrounding air lead to more significant fluctuations, as evident by an increase in the standard deviations, especially for the 3% O_2 case. At the 125mm location, additional variations are also noted with increased Reynolds number, as was previously observed in Table 3. The significant influence of Reynolds number on the 3% O_2 downstream data is an artefact of the increased turbulent stirring resulting in greater entrainment of surrounding air, subsequently leading to extinction events. **Naturally, the increased intermittency of the OH as a result of the extinction–reignition process leads to the increase in the standard deviation in the peak OH levels.**

The mean peak OH number density can be compared to laminar flame calculations. Calculations for both 3% and 9% O_2 oxidant streams (T_{oxi}=1100K) have been performed over a range of strain rates using the OPPDIF code of the Chemkin package and the GRI-Mech version 3.0 mechanism. **The results presented in Figure 13 show that the OH number density steadily increases with strain at low strain conditions, before levelling out for strain rates above approximately 100s^{-1}. In**

another set of laminar flame calculation (not presented here) at 21% O_2, and oxidant temperatures of both 300K and 1100K, the initial increase of peak OH with strain was noted at the 1100K case, but not evident at the lower air temperature case. The differences are directly attributed to the higher initial temperature.

Overlaid on Figure 13 are the experimental results from Table 4 for the 35mm location. It is apparent that there are noticeable variations in the OH number density of the experimental results and the laminar flame models. At 3% O_2 the model under-predicts the OH number density, whereas at 9% O_2 the experimental results are slightly below the maximum n_{OH} from the models. **The overlap between the experimental results and model for 9% O_2 indicates that 40s^{-1} typifies the average strain rate in the flames. These are nominally turbulent flows and this strain rate seems rather low, possibly implying an increased decay of turbulence levels under these hot diluted conditions.** The mooted concept of reduced turbulence levels under MILD conditions may be speculated to be as a result of the diminished thermal gradients across the reaction zone, further enhanced by the viscosity effects due to the elevated temperature of the oxidant stream. This inference is consistent with the previously noted observation of Re_{jet} having only minor influence on the mean and RMS radial profiles.

In the region where the OH number density is relatively independent on strain (i.e. for the high-end of strain rates on the plot), the differences between the experimental results and models are $\sim$20% for the 9% O_2 coflow and $\sim$50% for the 3% O_2 oxidant. Aside from the experimental errors, there may be uncertainties regarding the reliability of the kinetics under these non-conventional oxidant stream conditions, in particular for the 3% O_2 oxidant case.

The influence of surrounding air entrainment at the downstream (125mm) location on the OH levels in the instantaneous images has already been noted (§4.4). Particular attention is drawn to the instance of air entrainment in Figure 10b, where the OH number density is almost 3×10^{16} cm^{-3}. In comparison, over the entire range of strain rates (extending beyond those presented in Figure 13) the calculations suggest the OH number density not exceeding 2×10^{16} cm^{-3}, reiterating our intimation of the inclusion of higher O_2 levels leading to increases in OH concentration beyond that expected in the diluted conditions. This indicates the importance of ensuring homogeneous mixing under MILD combustion conditions, whereby inclusion of comparatively small amounts of fresh air, even at elevated temperatures due to mixing with the heated coflow, can lead to localised increases in reaction rates.

6 Conclusion

Turbulent nonpremixed CH_4/H_2 jet flames issuing into a heated and highly diluted coflow were investigated in this study. These conditions emulate those of MILD combustion conditions. Planar LIF and Rayleigh scattering are employed to simultaneously image the hydroxyl radical (OH), formaldehyde (H_2CO) and temperature for three different jet Reynolds numbers and two coflow O_2 levels at two downstream locations.

Decreasing the coflow O_2 level is shown to lead to a suppression of OH as a result of the reduced temperatures in the reaction zone. Associated with the drop in OH levels is a broadening of the OH layer. The less intense reaction zone at reduced O_2 levels leads to a greater degree of partial premixing in these flames which is evident through high H_2CO levels.

At downstream locations the influence of the coflow is diminished, enabling the surrounding air to mix with the jet and coflow. The associated drop in the temperature due to the entrained air can lead to localised extinction for the 3% O_2 coflow. The 9% O_2 coflow flames are more resilient to the cooling effects, but weakening of the OH is still noted. The less intense reaction zone as a result of cooling leads to premixing of the coflow with the surrounding air at downstream locations $\gtrsim$100mm for this JHC burner. The subsequent addition of oxygen leads to increases in reaction rates, thereby deviating from the MILD combustion regime. This has implications for furnace design, highlighting the need for homogeneous mixing to avoid localised high temperatures and the associated increases in NO_x emissions.

Acknowledgments

The authors would like to thank Dr Zeyad Alwahabi for his assistance with this project. The financial support of The University of Adelaide and the Australian Research Council is gratefully acknowledged.

References

[1] J. A. Wünning, J. G. Wünning, Flameless Oxidation to Reduce Thermal NO–formation, Prog. Energy Combust. Sci. 23 (1997) 81–94.

[2] A. Cavaliere, M. de Joannon, MILD Combustion, Prog. Energy Combust. Sci. 30 (2004) 329–366.

[3] J. G. Wünning, FLOX® — Flameless Combustion, in: Thermprocess Symposium 2003, WS Wärmeprozesstechnik GmbH, 2003.

[4] B. B. Dally, A. N. Karpetis, R. S. Barlow, Structure of Turbulent Non-Premixed Jet Flames in a Diluted Hot Coflow, Proc. Combust. Inst. 29 (2002) 1147–1154.

[5] C. Ahn, F. Akamatsu, M. Katsuki, A. Kitajima, The Influences of Mixture Composition and Preheat Temperature on Combustion Regime and Flame Structure of Premixed Turbulent Flames, in: The Fourth Asia–Pacific Conference on Combustion, 2003, pp. 40–43.

[6] B. B. Dally, A. N. Karpetis, R. S. Barlow, Structure of Jet Laminar Non-premixed Flames under Diluted Hot Coflow Conditions, in: 2002 Australian Symposium on Combustion and The Seventh Australian Flame Days, Adelaide, Australia, 2002.

[7] H. N. Najm, P. H. Paul, C. J. Mueller, P. S. Wyckoff, On the Adequacy of Certain Experimental Observables as Measurements of Flame Burning Rate, Combust. Flame 113 (1998) 312–332.

[8] P. R. Medwell, P. A. M. Kalt, B. B. Dally, Effect of Fuel Dilution on Jet Flames in a Heated and Diluted Co-flow, in: 5th Asia-Pacific Conference on Combustion, The University of Adelaide, Adelaide, Australia, 2005, pp. 325–328.

[9] P. R. Medwell, P. A. M. Kalt, B. B. Dally, Effect of Reynolds Number on the

Spatial Distribution of OH and Formaldehyde in Jet Flames in a Heated and Diluted Co-flow, in: 5th Asia-Pacific Conference on Combustion, The University of Adelaide, Adelaide, Australia, 2005, pp. 381–384.

[10] G. H. Dieke, H. M. Crosswhite, The Ultraviolet Bands of OH, J. Quant. Spectrosc. Radiat. Transfer 2 (1962) 97–199.

[11] P. H. Paul, H. N. Najm, Planar Laser-Induced Fluorescence Imaging of Flame Heat Release Rate, Proc. Combust. Inst. 27 (1998) 43–50.

[12] G. H. Dieke, G. B. Kistiakowsky, The Structure of the Ultraviolet Absorption Spectrum of Formaldehyde. I, Phys. Rev. 45 (1934) 4–28.

[13] H. S. P. Müller, G. Winnewisser, J. Demaison, A. Perrin, A. Valentin, The Ground State Spectroscopic Constants of Formaldehyde, J. Mol. Spectrosc. 200 (2000) 143–144.

[14] P. W. Atkins, Molecular Quantum Mechanics, 2nd Edition, Oxford University Press, 1983.

[15] B. Maessen, M. Wolfsberg, Variational Calculation of Lower Vibrational Energy Levels of Formaldehyde $\tilde{X}^1A_1$, J. Chem. Phys. 80 (10) (1984) 4651–4662.

[16] C. D. Carter, R. S. Barlow, Simultaneous Measurements of NO, OH, and the Major Species in Turbulent Flames, Opt. Lett. 19 (4) (1994) 299–301.

[17] N. L. Garland, D. R. Crosley, On the Collisional Quenching of Electronically Excited OH, NH and CH in Flames, Proc. Combust. Inst. 21 (1986) 1693–1702.

[18] P. R. Medwell, P. A. M. Kalt, B. B. Dally, Quantification of OH–LIF in Jet Diffusion Flames, in: Fourth Australian Conference on Laser Diagnostics in Fluid Mechanics and Combustion, The University of Adelaide, South Australia, Australia, 2005, pp. 105–108.

[19] B. O. Ayoola, R. Balachandran, J. F. Frank, E. Mastorakos, C. F. Kaminski,

Spatially Resolved Heat Release Rate Measurements in Turbulent Premixed Flames, Combust. Flame 114 (2006) 1–16.

[20] R. Bombach, B. Käppeli, Simultaneous Visualisation of Transient Species in Flames by Planar-Laser-Induced Fluorescence Using a Single Laser System, Appl. Phys. B 68 (1999) 251–255.

[21] K. Kohse-Höinghaus, J. B. Jeffries, Applied Combustion Diagnostics, Taylor & Francis, New York, 2002.

[22] C. S. McEnally, L. D. Pfefferle, Experimental Study of Nonfuel Hydrocarbon Concentrations in Coflowing Partially Premixed Methane/Air Flames, Combust. Flame 118 (1999) 619–632.

[23] C. S. McEnally, L. D. Pfefferle, Experimental Study of Nonfuel Hydrocarbons and Soot in Coflowing Partially Premixed Ethylene/Air Flames, Combust. Flame 121 (2000) 575–592.

[24] J. B. Kelman, A. R. Masri, Reaction Zone Structure and Scalar Dissipation Rates in Turbulent Diffusion Flames, Combust. Sci. Technol. 129 (1997) 17–55.

[25] T. Plessing, N. Peters, J. G. Wünning, Laseroptical Investigation of Highly Preheated Combustion with Strong Exhaust Gas Recirculation, Proc. Combust. Inst. 27 (1998) 3197–3204.

[26] M. P. Tolocka, J. H. Miller, Measurements of Formaldehyde Concentrations and Formation Rates in a Methane-Air, Non-Premixed Flame and Their Implications for Heat-Release, Proc. Combust. Inst. 27 (1998) 633–640.

[27] J. E. Harrington, K. C. Smyth, Laser-Induced Fluorescence Measurements of Formaldehyde in a Methane/Air Diffusion Flame, Chem. Phys. Lett. 202 (1993) 196–202.

[28] A. R. Masri, J. B. Kelman, B. B. Dally, The Instantaneous Spatial Structure Of The Recirculation Zone In Bluff-Body Stabilized Flames, Proc. Combust.

650 Inst. 27 (1998) 1031–1038.

Fuel	Re_{jet}	X_{O_2} (coflow)	Flame length
NG:H_2 (1:1)	5000	3%	1200mm
NG:H_2 (1:1)	10000	3%	1200mm
NG:H_2 (1:1)	15000	3%	1400mm
NG:H_2 (1:1)	5000	9%	600mm
NG:H_2 (1:1)	10000	9%	800mm
NG:H_2 (1:1)	15000	9%	1000mm

Table 1
List of flames and conditions.

Re_{jet}	3% O_2	9% O_2
5k	2.02mm	1.68mm
10k	2.04mm	1.81mm
15k	2.09mm	1.85mm

Table 2
Mean OH width estimates at 35mm downstream location for two coflow O_2 levels.

Re_{jet}	3% O_2	9% O_2
5k	1.5%	0%
10k	11.9%	0%
15k	33.7%	0%

Table 3
Proportion of images with evidence of extinction at 125mm location for two coflow O_2 levels.

OH number density $(\times 10^{16}\text{cm}^{-3})$ $[\sigma]$				
Location	Coflow	5k	10k	15k
35mm	3% O_2	0.67 [9%]	0.72 [10%]	0.70 [11%]
	9% O_2	1.55 [7%]	1.59 [9%]	1.60 [10%]
125mm	3% O_2	0.78 [22%]	0.93 [45%]	1.01 [52%]
	9% O_2	1.72 [11%]	1.77 [13%]	1.81 [16%]

Table 4
Mean and standard deviation (σ) of peak OH number density.

List of Figure Captions

Figure 1: Cross-sectional diagram of JHC burner.

Figure 2: Boltzmann population fractions for H_2CO ($X-$state, v''=0, J''=21, K''=6) and OH ($X-$state, v''=0, J''=7.5, Ω=$^3/_2$). Note different axes for each species.

Figure 3: Schematic of experimental layout.

Figure 4: Photographs of flames at two coflow O_2 levels with jet Reynolds numbers ranging from 5000 to 15000. Measurement locations are indicated by the horizontal lines. Photograph height 500mm. Note the different exposure times (other camera parameters constant).

Figure 5: **Axial location 35mm above jet exit – selection of instantaneous OH, H_2CO and temperature image triplets showing typical features (irrespective of Reynolds number). Each image 8$\times$30mm. Jet centreline marked with dashed line.**

Figure 6: **Axial location 35mm above jet exit – selection of instantaneous OH, H_2CO and temperature image triplets showing wide radial distribution of H_2CO. Each image 8$\times$30mm. Jet centreline marked with dashed line.**

Figure 7: **Effect of partial premixing on peak H_2CO mole fraction at two coflow O_2 levels.**

Figure 8: **Axial location 35mm above jet exit – mean and RMS radial profiles for OH, H_2CO and temperature at two coflow O_2 levels. Jet Reynolds numbers ranging from 5000 to 15000. Central 3mm portion of images used**.

Figure 9: **Axial location 125mm above jet exit – mean and RMS radial profiles for OH, H_2CO and temperature at two coflow O_2 levels. Jet Reynolds numbers ranging from 5000 to 15000. Central 3mm portion of images used**.

Figure 10: **Axial location 125mm above jet exit – selection of instantaneous OH, H_2CO and temperature image triplets showing effects of surrounding air entrainment. Each image 8$\times$30mm. Jet centreline marked with dashed line.**

Figure 11: **Axial location 125mm above jet exit – selection of instantaneous OH, H_2CO and temperature image triplets showing localised extinction events. Each image 8$\times$30mm. Jet centreline marked with dashed line.**

Figure 12: **Axial location 125mm above jet exit – selection of instantaneous OH, H_2CO and temperature image triplets showing effects of oxygen leakage. Each image 8$\times$30mm. Jet centreline marked with dashed line.**

Figure 13: Effect of strain on OH number density based on laminar flame models at two coflow O_2 levels. The overlaid horizontal dashed lines are the peak experimental results.

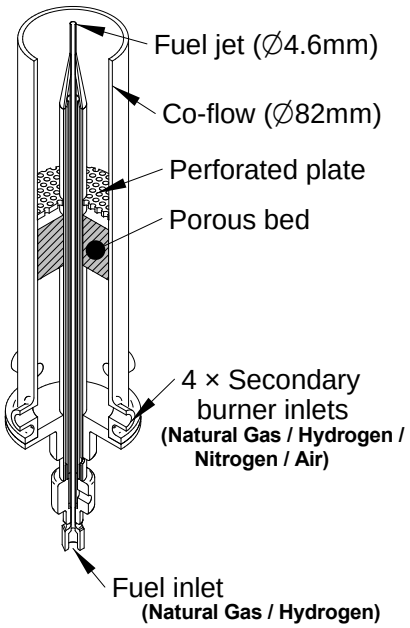

Fig. 1. Cross-sectional diagram of JHC burner.

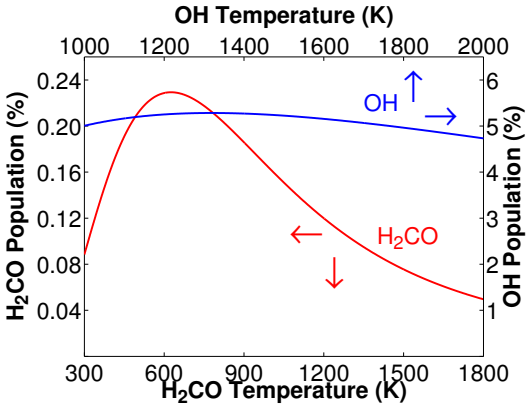

Fig. 2. Boltzmann population fractions for H_2CO ($X-$state, v''=0, J''=21, K''=6) and OH ($X-$state, v''=0, J''=7.5, Ω=$^3/_2$). Note different axes for each species.

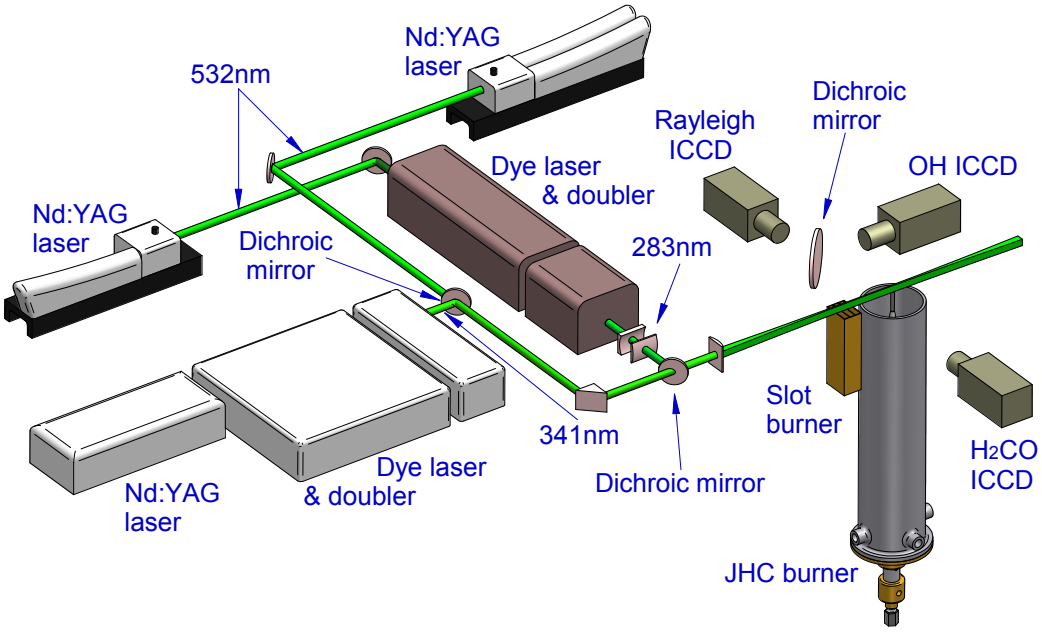

Fig. 3. Schematic of experimental layout.

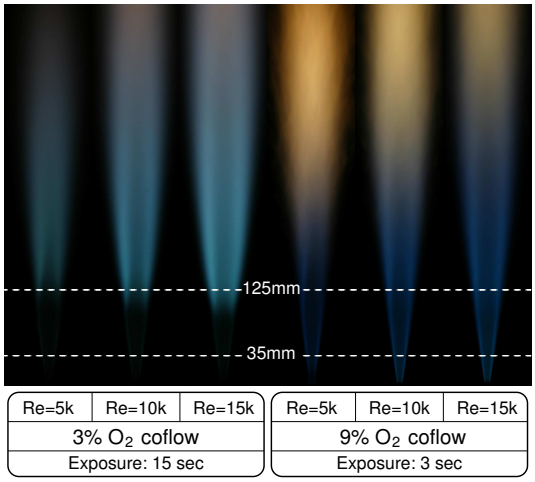

Fig. 4. Photographs of flames at two coflow O_2 levels with jet Reynolds numbers ranging from 5000 to 15000. Measurement locations are indicated by the horizontal lines. Photograph height 500mm. Note the different exposure times (other camera parameters constant).

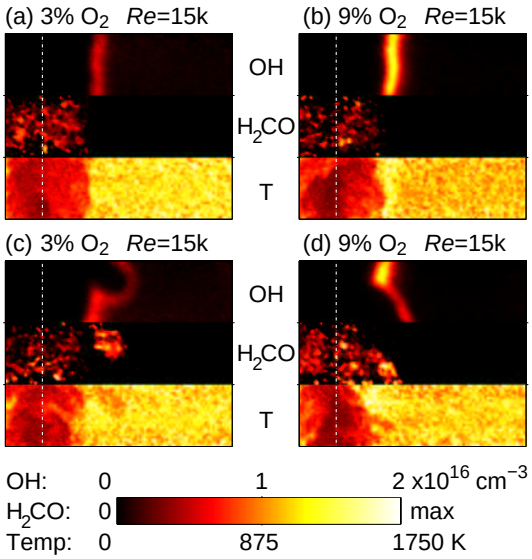

Fig. 5. **Axial location 35mm above jet exit – selection of instantaneous OH, H_2CO and temperature image triplets showing typical features (irrespective of Reynolds number). Each image 8×30mm. Jet centreline marked with dashed line.**

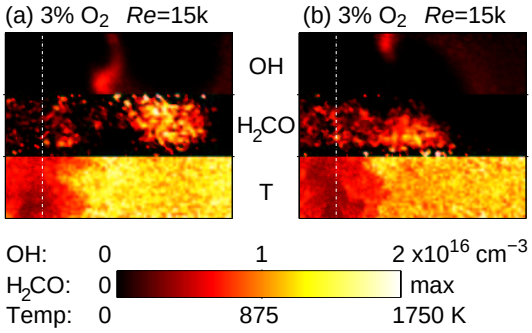

Fig. 6. **Axial location 35mm above jet exit – selection of instantaneous OH, H_2CO and temperature image triplets showing wide radial distribution of H_2CO. Each image 8×30mm. Jet centreline marked with dashed line.**

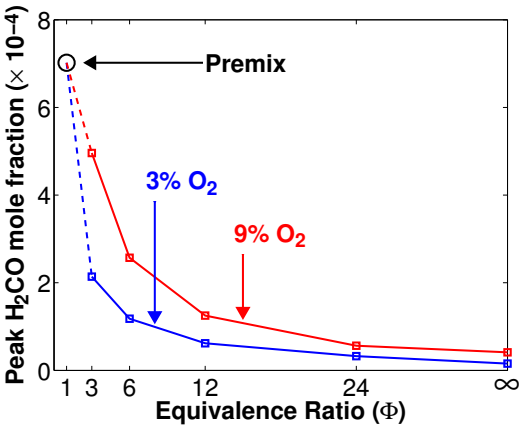

Fig. 7. **Effect of partial premixing on peak H_2CO mole fraction at two coflow O_2 levels.**

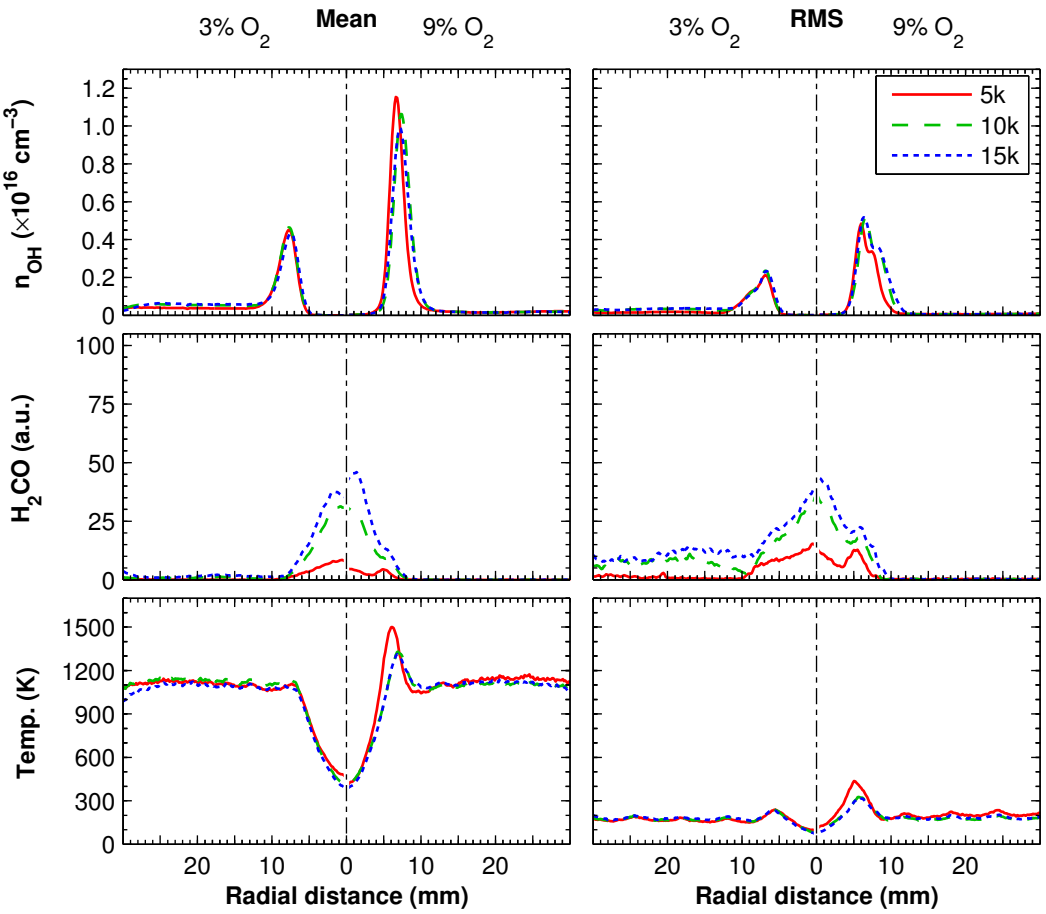

Fig. 8. **Axial location 35mm above jet exit – mean and RMS radial profiles for OH, H_2CO and temperature at two coflow O_2 levels. Jet Reynolds numbers ranging from 5000 to 15000. Central 3mm portion of images used**.

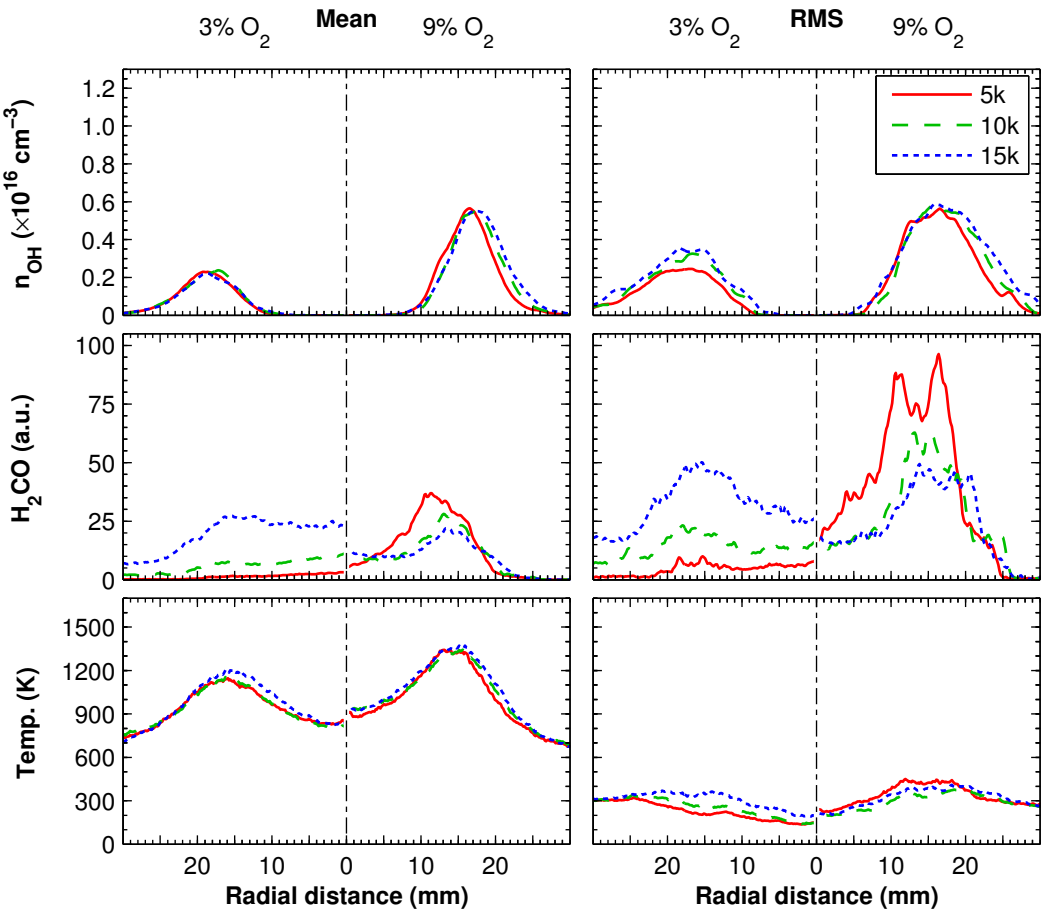

Fig. 9. **Axial location 125mm above jet exit – mean and RMS radial profiles for OH, H_2CO and temperature at two coflow O_2 levels. Jet Reynolds numbers ranging from 5000 to 15000. Central 3mm portion of images used**.

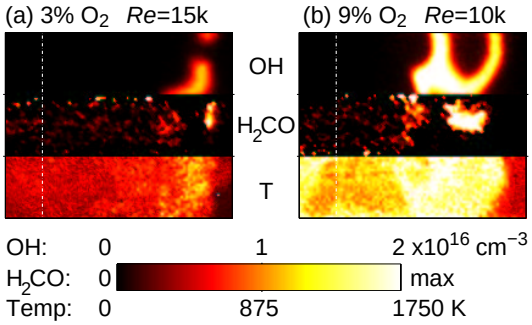

Fig. 10. **Axial location 125mm above jet exit – selection of instantaneous OH, H_2CO and temperature image triplets showing effects of surrounding air entrainment. Each image 8×30mm. Jet centreline marked with dashed line.**

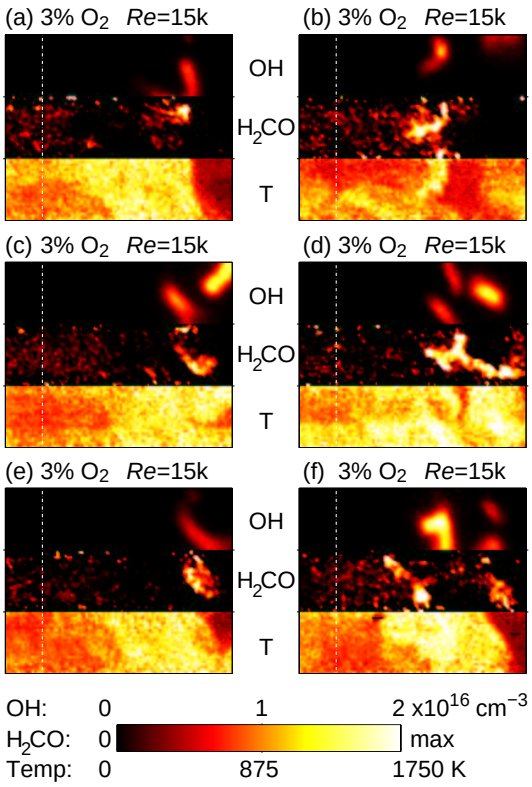

Fig. 11. **Axial location 125mm above jet exit – selection of instantaneous OH, H_2CO and temperature image triplets showing localised extinction events. Each image 8×30mm. Jet centreline marked with dashed line.**

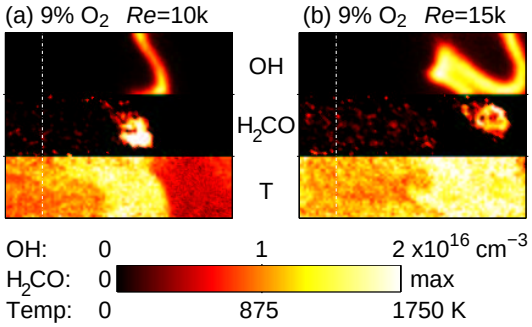

Fig. 12. **Axial location 125mm above jet exit – selection of instantaneous OH, H_2CO and temperature image triplets showing effects of oxygen leakage. Each image 8×30mm. Jet centreline marked with dashed line.**

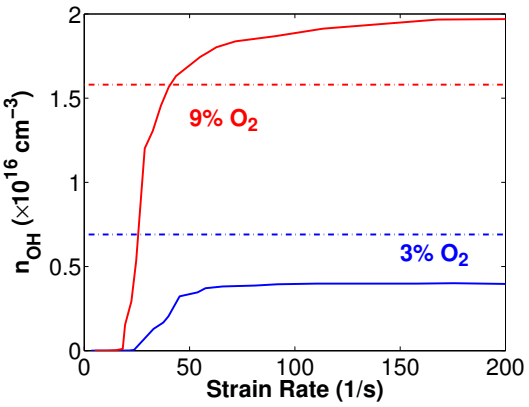

Fig. 13. Effect of strain on OH number density based on laminar flame models at two coflow O_2 levels. The overlaid horizontal dashed lines are the peak experimental results.